Kolzenburg, S., et al., 2021, Solid as a rock: Tectonic control of graben extension and dike propagation: Geology, https://doi.org/10.1130/G49406.1

Supplementary Material

S1. Chronology of Events During Rifting

The 2014–2015 rift event and eruption (Fig. 1 A–C) took place north of the Vatnajökull ice cap. Seismicity started on 16 August 2014 in the Bárðarbunga dike network and was tracked over a distance of ~50 km (Ágústsdóttir et al., 2019; Ágústsdóttir et al., 2016; Gudmundsson et al., 2016; Sigmundsson et al., 2015; Woods et al., 2018; Woods et al., 2019). Seismicity propagated from the Bárðarbunga caldera to the eruption site over 13 days preceding the eruption (Fig. 1E). Most earthquakes occurred during a northward propagation pulse between 26 and 31 August 2014, likely initiating graben subsidence (Ruch et al., 2016). The seismic front reached the eruption site two days before the first lava erupted and propagated ~1 km north beyond the eruption site (Woods et al., 2019). The first small eruption started on 29 August 2014 resulting in an immediate drop in seismicity. Seismicity briefly re-intensified as this eruption ceased and advanced north until the onset of the main eruption on 31 August 2014, when it reduced significantly.

The ~10 km long and 800 m wide graben was first observed during an airborne mission by the Icelandic coastguard on 27 August 2014 (Hjartardóttir et al., 2016; Ruch et al., 2016). It re-activated existing structures from a previous rifting and eruption event (Ruch et al., 2016). Lineations on the glacier indicate that the graben extends southward below the ice cap, which is also documented by different airborne and satellite remote sensing data (Hjartardóttir et al., 2016; Reynolds et al., 2017; Rossi et al., 2016; Ruch et al., 2016; Sigmundsson et al., 2015). Over the course of the eruption, this structure served as the plumbing system for a bulk erupted lava volume of 1.44 km^3, covering 84 km^2 between 29 August 2014 and 27 February 2015.

While seismicity in the caldera and throughout the entire dike dropped with initiation of the eruption, analysis of seismic tremor and long period events, correlated with magma movement, revealed significant pressure changes (i.e., dike inflation/deflation) in the plumbing system (Eibl et al., 2017b; Woods et al., 2018). Further, seismicity dynamics were directly correlated with the time-tveraged discharge rate (TADR; Fig. 1D) (Dumont et al., 2020; Eibl et al., 2017a). The TADR evolved from 320 to 10 m^3/s during the eruption and varied by up to 55% over a few days (Coppola et al., 2017; Pedersen et al., 2017). Ground based measurements suggest even higher TADR values of up to 560 m^3/s and fluctuation of up to 90% in the early eruption phase (Bonny et al., 2018).

Several minor eruptions occurred along the dike before the main eruption (Sigmundsson et al., 2015). This is documented in three ice cauldrons on the glacier, each marking small, subglacial eruptions (Reynolds et al., 2017) and the short-lived subaerial eruption on 29 August 2014. Thus, the dike had breached the surface repeatedly prior to reaching the main eruption site, allowing it to release overpressure and generating pressure pulses throughout the plumbing system.

In summary, both effusion rate and seismic data (Fig. 1D,E) document heavily pulsating dynamics within the magma plumbing system throughout the eruption, indicative of changes in magma pressure and transport velocity, linked to dike inflation and deflation.

S2. Digital Elevation Model (DEM) Processing

S2.1. TanDEM-X dataset

The TanDEM-X Co-Registered Single Look Slant Range Complex (CoSSC) data used in this study were made available within the framework of the project Iceland subglacial Volcanoes

interdisciplinary early warning system (IsViews) leaded by U. Münzer LMU Munich (TanDEM-X Science Proposal “Other 2375”, PI: C. Minet) and TanDEM-X Science Proposal “NTI _INSA0405” (PI: M. Westerhaus). Overall, the CoSSC data allowed processing a total of seven TanDEM-X Digital Elevation Models (DEMs; Table 1). In addition, a global TanDEM-X DEM tile was available under Proposal “DEM_GEOL1270”; Project IsViews (Münzer et al., 2016). The acquisitions were selected to cover the whole period of the Bárðarbunga eruption and associated rifting in 2014–2015. The global DEM tile as well as the 27 May 2014 TanDEM-X DEM (Table 1) represent the surface conditions before graben formation and the remaining DEMs cover the period during and after the 2014–2015 Bárðarbunga volcanic eruption. The raw DEMs were processed from monostatic and bistatic Synthetic Aperture Radar (SAR) data using either the integrated TanDEM-X processor (ITP) at the German Aerospace Center (DLR) or a modified version of the Delft Object-Oriented Radar Interferometric Software, DORIS (Kampes et al., 2003; Kubanek et al., 2015). In contrast, the global DEM tile was generated from multi-temporal TanDEM-X DEMs covering the period 2011–2014. The use of multi-temporal DEMs with varying acquisition geometries allowed increasing the overall accuracy of the global DEM. The spatial extent of the TanDEM-X raw DEMs was either 50 km × 30 km or 30 km × 30 km and the dimension of the global DEM tile was around 111 km × 111 km. Finally, the horizontal sampling of the products was approximately 6 m in northing and easting for the raw DEMs and 12 m along both directions for the global DEM tile.

S2.1.1 DEM Quality

The accuracy of InSAR DEMs is mainly impacted by the SAR acquisition geometry, environmental conditions such as topography, the relative movement of objects, volumetric scattering, and DEM processing methods (Bamler and Hartl, 1998; Hanssen, 2001). To assign a

numerical value to the assessment of DEM quality, the interferometric coherence γ or the DEM standard error h_{err} is calculated (Bamler and Hartl, 1998; Hanssen, 2001; Martone et al., 2012; Rizzoli et al., 2012). The interferometric coherence reflects the correlation between two SAR images. The DEM standard error measures the amount of spatial decorrelation in dependence of the local coherence and the height of ambiguity; i.e., the altitude difference corresponding to a phase (Bamler and Hartl, 1998; Martone et al., 2012; Rizzoli et al., 2012; Rossi et al., 2016). The height error (also referred to as DEM standard error) measures the amount of spatial correlation in dependence of the local coherence and the height of ambiguity:

$$h_{err}(r,a) = \sigma_{\phi}(r,a)\frac{h_{amb}}{2\pi}$$

where σ_{ϕ} is the standard deviation of the interferometric phase for each sample in azimuth and range and h_{amb} is the height of ambiguity. The height error is provided pixel-wise for each DEM dataset. To retrieve the mean height error for each TanDEM-X acquisition, the height error map was averaged.

Table S1 gives an overview of the geometric and quality parameters of the selected TanDEM-X dataset. Since our study area is situated in a flat, vegetation-free glacial outwash plain (Baratoux et al., 2011; Mountney and Russell, 2004), environmental processes were not believed to have affected DEM quality. Considering this, the only remaining factors to address are the SAR geometry and the SAR processing. While most investigated acquisitions show an overall good mean coherence (> 0.75) and low mean height error (≤ 0.5 m), the 22 June 2015 acquisition suffers from a slightly reduced mean coherence (0.66). This is the result of its acquisition geometry and consequent problems in the SAR processing. In fact, the large perpendicular baseline $B_{\perp}$ (i.e., the distance between two satellites projected perpendicular to the

slant range direction), and the resultant low height of ambiguity h_a (i.e., the height difference between two adjacent discontinuities), led to errors in the phase unwrapping processing step. This is also reflected in the low-quality ratio (87.1), a measure indicating the percentage of correctly unwrapped pixels in a DEM (Rossi et al., 2012). During InSAR DEM generation, phase unwrapping describes the process of adding the correct integer multiple of 2π to the interferometric fringes (Ferretti et al., 2007). However, phase unwrapping did not affect our area of interest within the full DEM scene and the acquisition can be used without problems.

The mean height error of the 9 September 2014 acquisition is larger than for the rest of the dataset (2.3 m). Here, a low perpendicular baseline led to a larger height of ambiguity. Even though the large height of ambiguity facilitated the phase unwrapping procedure (q_r = 99.9), the resultant DEM contains a considerable level of noise and can only be used with caution or adequate filtering. For this purpose, we smoothed the 9 September 2014 DEM with a low pass Gaussian filter.

Table S1. Acquisition geometry and quality parameters of the TanDEM-X dataset used in the study. $B_\perp$, h_a, θ, $\bar{\gamma}$, $\bar{h}_{err}$ and q_r are the perpendicular baseline, the height of ambiguity, the center radar incidence angle, the mean coherence over the entire TanDEM-X scene, the mean height error over the entire TanDEM-X scene and the quality ratio respectively.

Acquisition date (Day.Month.Year)	$B_\perp$ [m]	h_a [m]	θ [deg]	$\bar{\gamma}$	$\bar{h}_{err}$ [m]	q_r	Acquisition mode
27.05.2014	175.7	39.5	41.5	0.65	–	–	Bistatic
09.09.2014	41.8	142.9	37.1	0.87	2.3	99.9	Bistatic
06.12.2014	148.1	42.2	37.3	0.86	0.5	99.9	Monostatic
22.12.2014	338.9	21.6	42.8	0.84	0.4	99.9	Monostatic
13.01.2015	549.0	13.2	42.8	0.82	0.2	98.0	Monostatic
26.02.2015	611.1	11.8	42.8	0.76	0.3	98.8	Monostatic
22.06.2015	576.5	10.5	37.1	0.66	0.3	87.1	Bistatic

The overall high accuracy of the dataset and the absence of significant DEM errors for almost all acquisitions make this dataset highly suitable for our study. While this represents only a short description of the general characteristics of the present dataset, a more in-depth revision of the basic theory of InSAR, DEM generation and factors leading to DEM errors are described in the literature e.g., (Bamler and Hartl, 1998; Ferretti et al., 2007; Hanssen, 2001). Dirscherl and Rossi (2018) moreover provide a detailed description of most investigated acquisitions and relevant sources of error over the study area.

S2.1.2 DEM post-processing

DEM differencing is a well-recognized approach for the computation of temporal elevation changes over volcanic edifices and is based upon the subtraction of two or more multi-temporal DEMs covering the same region (Albino et al., 2015; Dirscherl and Rossi, 2018; Kubanek et al., 2017; Kubanek et al., 2015; Poland, 2014; Rossi et al., 2016). The comparison of time-sequential DEMs of the same spatial location requires the correct horizontal and vertical alignment (co-registration) of the investigated data. While absolute height offsets are difficult to account for without additional elevation reference, relative phase offsets can be easily determined defining a common reference out of the available data (Dirscherl and Rossi, 2018; Rossi et al., 2016).

To investigate geomorphological changes during the graben formation associated with the 2014–2015 Bárðarbunga eruption, DEM differencing has been applied to all TanDEM-X, UltraCam and drone-based DEMs described above and in the main manuscript. Since the principal matter of interest of our study was the geomorphological development of the Holuhraun graben compared to pre-eruptive conditions, an absolute height calibration was not necessary and only relative changes in elevation were considered. Relative elevation offsets were quantified in terms of average height values over selected stable terrain portions (e.g., rock outcrops, sandur surfaces) and with respect to the global TanDEM-X DEM. The vertical alignment of the DEMs was subsequently integrated into the DEM differencing step by adding or subtracting the detected offsets from the respective layers. To visualize the result, difference maps as well as transverse profiles were created and are shown in Fig. 2–4.

In a last procedure, the accuracy of the DEM relative calibration was evaluated following the approach used in Dirscherl and Rossi (2018), Poland (2014), Xu and Jónsson (2014), and Kubanek et al. (2017). For this purpose, the correct overlay of transects in stable terrain portions

as well as the statistical distribution of elevation difference values in selected control areas within the glacial outwash plain around the fracture zone were analysed. For a correct vertical calibration, the average height difference within the control areas is expected to be near 0 m. As reported in Table S2, this was in fact the case for all control areas and difference maps under study. At the same time, we found slightly increased values for the average standard deviation. This is in agreement with the findings in Dirscherl and Rossi (2018) and most likely results from the periodic and spatially variable flooding of the sandur plain. The maximum detected standard deviation was found at 1.04 m, mainly because of an increased value of the 09 September 2014 acquisition.

Table S2. Statistical evaluation of the DEM vertical calibration with respect to the global TanDEM-X DEM. Overall mean μ and standard deviation σ of selected control areas in the difference maps over the Holuhraun graben.

Control area	μ [m]	σ [m]
1	0.41	1.04
2	0.38	0.61
3	0.32	0.58
4	0.51	0.73

S2.2. UltraCam-Xp dataset

In addition to the TanDEM-X DEMs, very high spatial resolution (20 cm/pixel) UltraCam Xp data (Gruber et al., 2008; Wiechert et al., 2011) were acquired on 29 August 2014 (i.e., the beginning of the eruption) and 6 September 2015. This is an airborne instrument that was flown at an altitude of 5100 m, creating a ground sampling distance of ~20-25 cm. A total of 457 stereo images were used to create the DEM and orthophoto mosaics (OMs) at a resolution of ~20 cm/pixel. The data were used to interpret the extent and temporal dynamics of the graben

feature on an OM and for verification of the TanDEM-X data. Unfortunately, the mission on 29 August 2014 had to be aborted early and hence only a small area is covered by the data (see Figure 2A).

The aerial UltraCam-Xp images were processed with the software packages match-at (Inpho) and SURE (NFrames). Aerotriangulation (also known as bundle block adjustment) was carried out using match-at software (Albertz and Wiggenhagen, 2009) and at least 20 tie points were identified per image. The co-registered (GPS) and inertial navigation system (INS) data were integrated into the aerotriangulation and hence the processing did not require any further ground control points. The semi-global-matching (SGM) algorithm (Heipke, 2017; Hirschmüller, 2011) was used to generate a dense point cloud from the oriented aerial imagery. The subsequent generation of the DEM and OM from the dense point cloud was carried out using SURE software. The final DEM was co-registered to the TanDEM-X global DEM using the DEM differencing approach outlined in the previous section.

S2.3. Small Unoccupied Aircraft System (sUAS) data

Data were collected over the Holuhraun graben on 31 July 2019 using a Trimble UX5-HP small Unoccupied Aircraft System (sUAS). The UX5-HP is a fixed-wing sUAS equipped with 36.4 MP Sony α7R full-frame mirrorless digital camera and an integrated Global Navigation Satellite System (GNSS) receiver. Simultaneous measurements acquired using a Trimble R10 GNSS base station enabled differential GPS corrections of the aircraft positions using Post Processed Kinematic (PPK) workflow.

Trimble Aerial Imaging software was used to plan and execute the flights, acquiring digital photographs in a regular grid pattern with 80% overlap along track and between adjacent

flight lines. The launch point (16°51’8” W and 64°51’41” N) was located at an elevation of 745 m and sUAS was directed toward higher elevation terrain to the south. Relative to the launch point, the UX5-HP flew at an altitude of 100 m above and the camera was configured with a 15 mm (wide-angle) fixed focal length lens. The altitude and lens parameters were expected to yield digital photographs (N = 480) with a GSD of ~4.88 cm. Before flight, 18 Ground Control Points (GCPs) were distributed within the survey area and were each geolocated using a Trimble R10 GNSS receiver operating as a mobile rover. All differential GPS and sUAS measurements were processed using Trimble Business Center (TBC) version 3.7. TBC is a proprietary software solution for post-processing GNSS surveys and includes an integrated Aerial Photogrammetry Module (APM) that offers an Advanced UAS option for the UX5-HP. APM completes all major post-processing steps, including refinement of flight trajectories using PPK localization; camera and lens calibrations; calculations of interior and exterior camera position orientations; bundle adjustment; automatic tie point estimation; dense 3D point matching; and the computation of the final data products. TBC outputs included for the graben survey include a dense point cloud with a post spacing of 10 cm, a digital terrain model (DTM) with a grid spacing of 15.7 cm, and an orthomosaic with a pixel scale = 3.13 cm. On 1 August 2019, the coordinates for 18 GCPs were collected in the field using the Trimble R10. The GCPs were located in the orthomosaic and used to extract positions within the DTM, yielding a root mean square error (RMSE) of x = 4.4 cm, y = 4.0 cm, z = 2.9 cm, for latitude, longitude, and elevation (relative to the ISN2004 datum), respectively. Profile C (Figs. 3 and 4) was then extracted from the DTM along a transect running from 16°51’39.534” W and 64°51’2.619” N to 16°50’18.844” W and 64°50’49.14” N. The final DEM was co-registered to the TanDEM-X global DEM using the DEM differencing approach outlined in the section on the TanDEM-X dataset (S2.1).

S3. Structural Mapping of Surface Fractures

To evaluate the stress field acting during graben formation as well as its potential evolution with time we generated detailed maps of all fractures visible in the orthophotos generated from the UltraCam-Xp data acquired on 29 August 2014 and 6 September 2015 (Fig. S1). The orthophotos have a very high spatial scale of 20 cm/pixel, enabling us to capture the surface structures of graben formation over a vast area in unprecedented detail. All individual fracture segments were digitally mapped in a Geographic Information System (GIS) environment, and their lengths and orientations (azimuths) were recorded. This dataset includes the most pristine record of surface fractures associated to the graben formation and probably the most complete dataset published of any graben formation to date, as it samples the fracture pattern during the final stage of active graben formation. In total, over 9200 individual fracture segments were mapped. Note that the vast majority of those are identified in the UltraCam Xp data acquired on 29 August 2014. This is because: (1) much of the graben feature was infilled by lava during the eruption and is thus no longer visible in the dataset from 6 September 2015; and (2) the high activity of aeolian sediment transport in the glacial outwash plain had filled in many smaller fractures by 6 September 2015. However, the main fracture systems defining the graben remain easily identifiable (Fig. S1).

Rose diagrams showing the orientation and frequency of fractures identified in and around the graben are shown in Fig. S2 A and B for the UltraCam-Xp data of 29 August 2014 and 6 September 2015, respectively. The diagrams were produced using GeoRose (Yong, 2015).

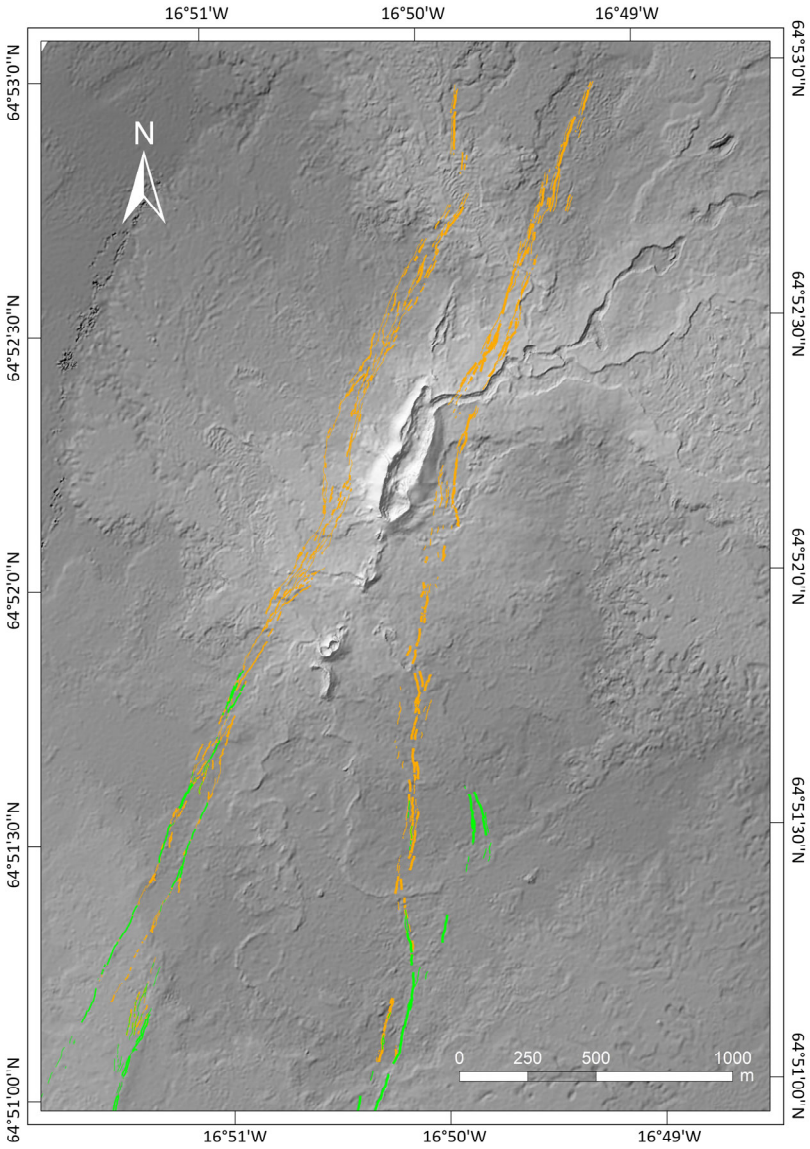

Figure S1. Faults mapped in the area covered by UltraCam-Xp data of 29 August 2014 (orange) and 6 September 2015 (green). There is no lateral shift in fracture locations, indicating a stable graben architecture after initial formation. Note that the northern portion of the area was covered by lava during the eruption, hence there are no fractures visible in that area in the 2015 images.

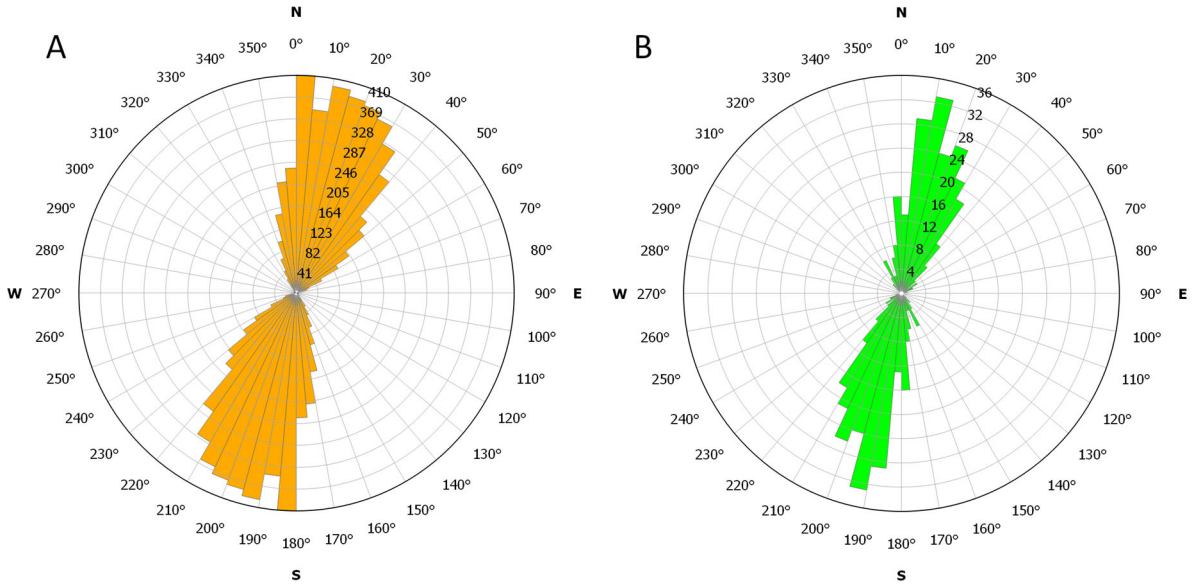

Figure S2. Rose diagrams in subplots A and B show fracture orientation and frequency in the area shown in Fig. 1S, measured on the UltraCam-Xp data of 29 August 2014 and 6 September 2015, respectively. Note that many more faults were mapped in 2014, as the northern part of the area was covered by lava during the eruption.

References Cited

Ágústsdóttir, T., Winder, T., Woods, J., White, R. S., Greenfield, T., and Brandsdóttir, B., 2019, Intense Seismicity During the 2014–2015 Bárðarbunga-Holuhraun Rifting Event, Iceland, Reveals the Nature of Dike-Induced Earthquakes and Caldera Collapse Mechanisms: Journal of Geophysical Research: Solid Earth, v. 124, no. 8, p. 8331-8357.

Ágústsdóttir, T., Woods, J., Greenfield, T., Green, R. G., White, R. S., Winder, T., Brandsdóttir, B., Steinthórsson, S., and Soosalu, H., 2016, Strike-slip faulting during the 2014 Bárðarbunga-Holuhraun dike intrusion, central Iceland: Geophysical Research Letters, v. 43, no. 4, p. 1495-1503.

Albertz, J., and Wiggenhagen, M., 2009, Taschenbuch zur Photogrammetrie und Fernerkundung, Wichmann Heidelberg, Germany.

Albino, F., Smets, B., d'Oreye, N., and Kervyn, F., 2015, High-resolution TanDEM-X DEM: An accurate method to estimate lava flow volumes at Nyamulagira Volcano (DR Congo): Journal of Geophysical Research: Solid Earth, v. 120, no. 6, p. 4189-4207.

Bamler, R., and Hartl, P., 1998, Synthetic aperture radar interferometry: Inverse Problems, v. 14, no. 4, p. R1-R54.

Baratoux, D., Mangold, N., Arnalds, O., Bardintzeff, J. M., Platevoet, B., Grégoire, M., and Pinet, P., 2011, Volcanic sands of Iceland-Diverse origins of aeolian sand deposits revealed at Dyngjusandur and Lambahraun: Earth Surface Processes and Landforms, v. 36, no. 13, p. 1789-1808.

Bonny, E., Thordarson, T., Wright, R., Höskuldsson, A., and Jónsdóttir, I., 2018, The Volume of Lava Erupted During the 2014 to 2015 Eruption at Holuhraun, Iceland: A Comparison Between Satellite- and Ground-Based Measurements: Journal of Geophysical Research: Solid Earth, v. 123, no. 7, p. 5412-5426.

Coppola, D., Ripepe, M., Laiolo, M., and Cigolini, C., 2017, Modelling satellite-derived magma discharge to explain caldera collapse: Geology, p. G38866. 38861.

Dirscherl, M., and Rossi, C., 2018, Geomorphometric analysis of the 2014–2015 Bárðarbunga volcanic eruption, Iceland: Remote Sensing of Environment, v. 204, p. 244-259.

Dumont, S., Le Mouël, J.-L., Courtillot, V., Lopes, F., Sigmundsson, F., Coppola, D., Eibl, E. P., and Bean, C. J., 2020, The dynamics of a long-lasting effusive eruption modulated by Earth tides: Earth and Planetary Science Letters, v. 536, p. 116145.

Eibl, E. P., Bean, C. J., Jónsdóttir, I., Höskuldsson, A., Thordarson, T., Coppola, D., Witt, T., and Walter, T. R., 2017a, Multiple coincident eruptive seismic tremor sources during the 2014–2015 eruption at Holuhraun, Iceland: Journal of Geophysical Research: Solid Earth, v. 122, no. 4, p. 2972-2987.

Eibl, E. P., Bean, C. J., Vogfjörd, K. S., Ying, Y., Lokmer, I., Möllhoff, M., O'Brien, G. S., and Pálsson, F., 2017b, Tremor-rich shallow dyke formation followed by silent magma flow at Bárðarbunga in Iceland: Nature Geoscience, v. 10, no. 4, p. 299-304.

Ferretti, A., Monti-Guarnieri, A., Prati, C., and Rocca, F., 2007, InSAR Principles: Guidelines for SAR Interferometry Processing and Interpretation, 19 vols: The Netherlands: ESA Publications.

Gruber, M., Ponticellia, M., Bernögger, S., and Leberl, L., UltraCamX, the large format digital aerial camera system by Vexcel Imaging/Microsoft, *in* Proceedings Proceedings of ISPRS XXIst Congress "Silk Road for Information from Imagery2008, p. 3-11.

Gudmundsson, M. T., Jónsdóttir, K., Hooper, A., Holohan, E. P., Halldórsson, S. A., Ófeigsson, B. G., Cesca, S., Vogfjörd, K. S., Sigmundsson, F., and Högnadóttir, T., 2016, Gradual caldera collapse at Bárdarbunga volcano, Iceland, regulated by lateral magma outflow: Science, v. 353, no. 6296, p. aaf8988.

Hanssen, R. F., 2001, Radar interferometry: data interpretation and error analysis, Springer Science & Business Media.

Heipke, C., 2017, Photogrammetrie und Fernerkundung: Handbuch der Geodäsie, herausgegeben von Willi Freeden und Reiner Rummel, Springer.

Hirschmüller, H., 2011, Semi-global matching-motivation, developments and applications: Photogrammetric Week 11, p. 173-184.

Hjartardóttir, Á. R., Einarsson, P., Gudmundsson, M. T., and Högnadóttir, T., 2016, Fracture movements and graben subsidence during the 2014 Bárðarbunga dike intrusion in Iceland: Journal of Volcanology and Geothermal Research, v. 310, p. 242-252.

Kampes, B. M., Hanssen, R. F., and Perski, Z., Radar interferometry with public domain tools, *in* Proceedings Proceedings of FRINGE2003, Volume 3.

Kubanek, J., Westerhaus, M., and Heck, B., 2017, TanDEM-X time series analysis reveals lava flow volume and effusion rates of the 2012–2013 Tolbachik, Kamchatka fissure eruption: Journal of Geophysical Research: Solid Earth, v. 122, no. 10, p. 7754-7774.

Kubanek, J., Westerhaus, M., Schenk, A., Aisyah, N., Brotopuspito, K. S., and Heck, B., 2015, Volumetric change quantification of the 2010 Merapi eruption using TanDEM-X InSAR: Remote Sensing of Environment, v. 164, p. 16-25.

Martone, M., Bräutigam, B., Rizzoli, P., Gonzalez, C., Bachmann, M., and Krieger, G., 2012, Coherence evaluation of TanDEM-X interferometric data: ISPRS Journal of Photogrammetry and Remote Sensing, v. 73, p. 21-29.

Mountney, N. P., and Russell, A. J., 2004, Sedimentology of cold-climate aeolian sandsheet deposits in the Askja region of northeast Iceland: Sedimentary Geology, v. 166, no. 3-4, p. 223-244.

Münzer, U., Jaenicke, J., Eineder, M., Minet, C., Braun, L., Mayer, C., Siegert, F., and Franke, J., 2016, Anwendung neuer Methoden mit hochauflösenden Fernerkundungsdaten (TerraSAR-X, TanDEM-X, RapidEye, UltraCam, HRSC) zur Früherkennung subglazialer Vulkanausbrüche auf Island. pp.1-85, http://www.isviews.geo.uni-muenchen.de

Pedersen, G. B. M., Höskuldsson, A., Dürig, T., Thordarson, T., Jónsdóttir, I., Riishuus, M. S., Óskarsson, B. V., Dumont, S., Magnusson, E., Gudmundsson, M. T., Sigmundsson, F., Drouin, V. J. P. B., Gallagher, C., Askew, R., Guðnason, J., Moreland, W. M., Nikkola, P., Reynolds, H. I., and Schmith, J., 2017, Lava field evolution and emplacement dynamics of the 2014–2015 basaltic fissure eruption at Holuhraun, Iceland: Journal of Volcanology and Geothermal Research.

Poland, M. P., 2014, Time-averaged discharge rate of subaerial lava at Kīlauea Volcano, Hawai ‘i, measured from TanDEM-X interferometry: Implications for magma supply and storage during 2011–2013: Journal of Geophysical Research: Solid Earth, v. 119, no. 7, p. 5464-5481.

Reynolds, H. I., Gudmundsson, M. T., Högnadóttir, T., Magnússon, E., and Pálsson, F., 2017, Subglacial volcanic activity above a lateral dyke path during the 2014–2015 Bárdarbunga-Holuhraun rifting episode, Iceland: Bulletin of Volcanology, v. 79, no. 6, p. 38.

Rizzoli, P., Bräutigam, B., Kraus, T., Martone, M., and Krieger, G., 2012, Relative height error analysis of TanDEM-X elevation data: ISPRS Journal of Photogrammetry and Remote Sensing, v. 73, p. 30-38.

Rossi, C., Gonzalez, F. R., Fritz, T., Yague-Martinez, N., and Eineder, M., 2012, TanDEM-X calibrated raw DEM generation: ISPRS Journal of Photogrammetry and Remote Sensing, v. 73, p. 12-20.

Rossi, C., Minet, C., Fritz, T., Eineder, M., and Bamler, R., 2016, Temporal monitoring of subglacial volcanoes with TanDEM-X—Application to the 2014–2015 eruption within the Bárðarbunga volcanic system, Iceland: Remote Sensing of Environment, v. 181, p. 186-197.

Ruch, J., Wang, T., Xu, W., Hensch, M., and Jónsson, S., 2016, Oblique rift opening revealed by reoccurring magma injection in central Iceland: Nature Communications, v. 7, no. 1, p. 12352.

Sigmundsson, F., Hooper, A., Hreinsdóttir, S., Vogfjörd, K. S., Ófeigsson, B. G., Heimisson, E. R., Dumont, S., Parks, M., Spaans, K., and Gudmundsson, G. B., 2015, Segmented lateral dyke growth in a rifting event at Barðarbunga volcanic system, Iceland: Nature, v. 517, no. 08 January 2015, p. 191-195.

Wiechert, A., Gruber, M., and Ponticelli, M., UltraCam: the new superlarge format digital aerial camera, *in* Proceedings Proc. of the ASPRS 2011 Annual Conference, Milwaukee, Wisconsin2011.

Woods, J., Donaldson, C., White, R. S., Caudron, C., Brandsdóttir, B., Hudson, T. S., and Ágústsdóttir, T., 2018, Long-period seismicity reveals magma pathways above a laterally propagating dyke during the 2014–15 Bárðarbunga rifting event, Iceland: Earth and Planetary Science Letters, v. 490, p. 216-229.

Woods, J., Winder, T., White, R. S., and Brandsdóttir, B., 2019, Evolution of a lateral dike intrusion revealed by relatively-relocated dike-induced earthquakes: The 2014–15 Bárðarbunga–Holuhraun rifting event, Iceland: Earth and Planetary Science Letters, v. 506, p. 53-63.

Xu, W., and Jónsson, S., 2014, The 2007–8 volcanic eruption on Jebel at Tair island (Red Sea) observed by satellite radar and optical images: Bulletin of Volcanology, v. 76, no. 2, p. 1-14.

Yong, 2015, Yong Technologies Inc. GeoRose 0.4. 3–Rose Plot Software.

Fig. S1

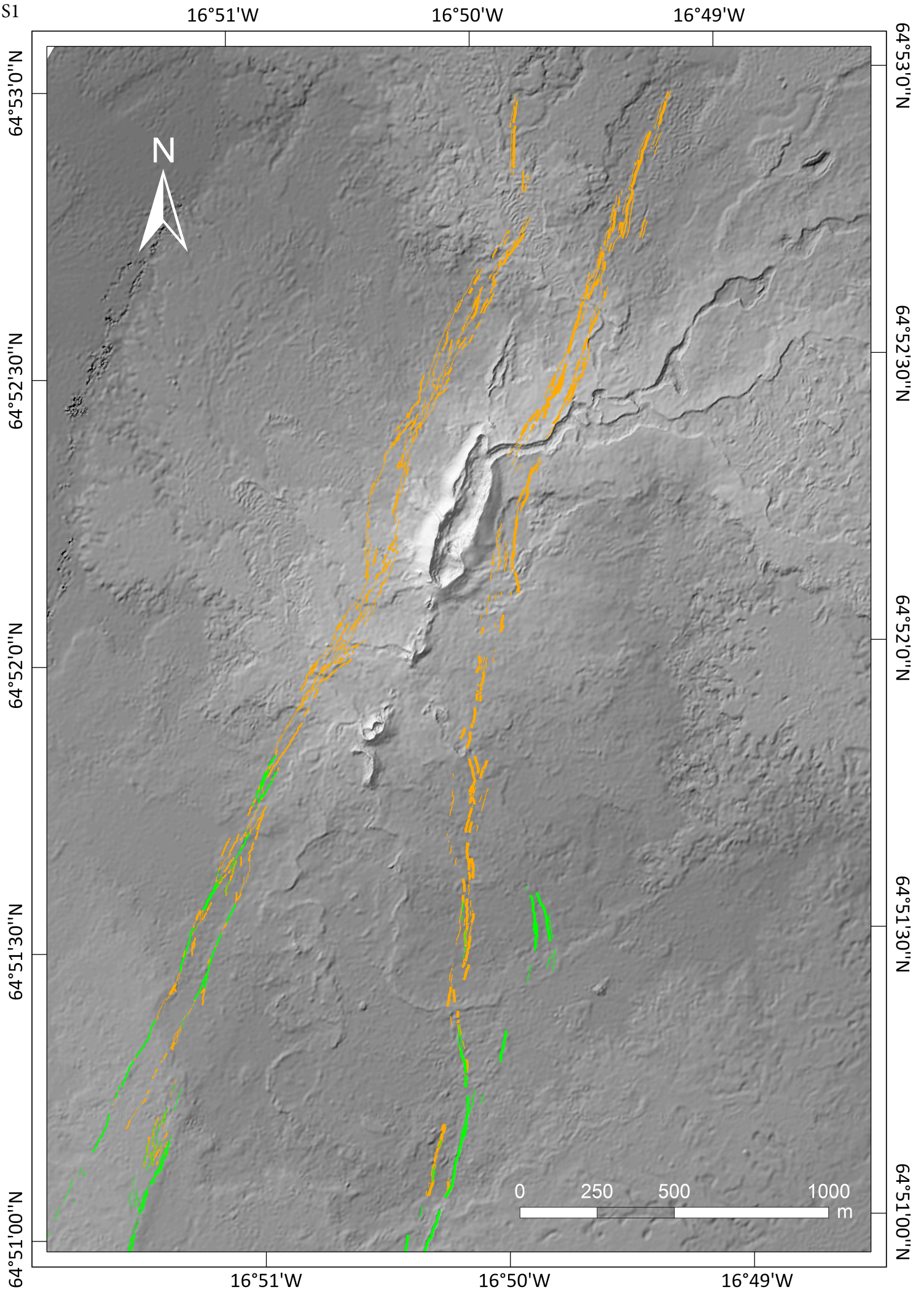
16°51'W
16°50'W
16°49'W
64°53'0"N
64°52'30"N
64°52'0"N
64°51'30"N
64°51'00"N
N
0
250
500
1000
m

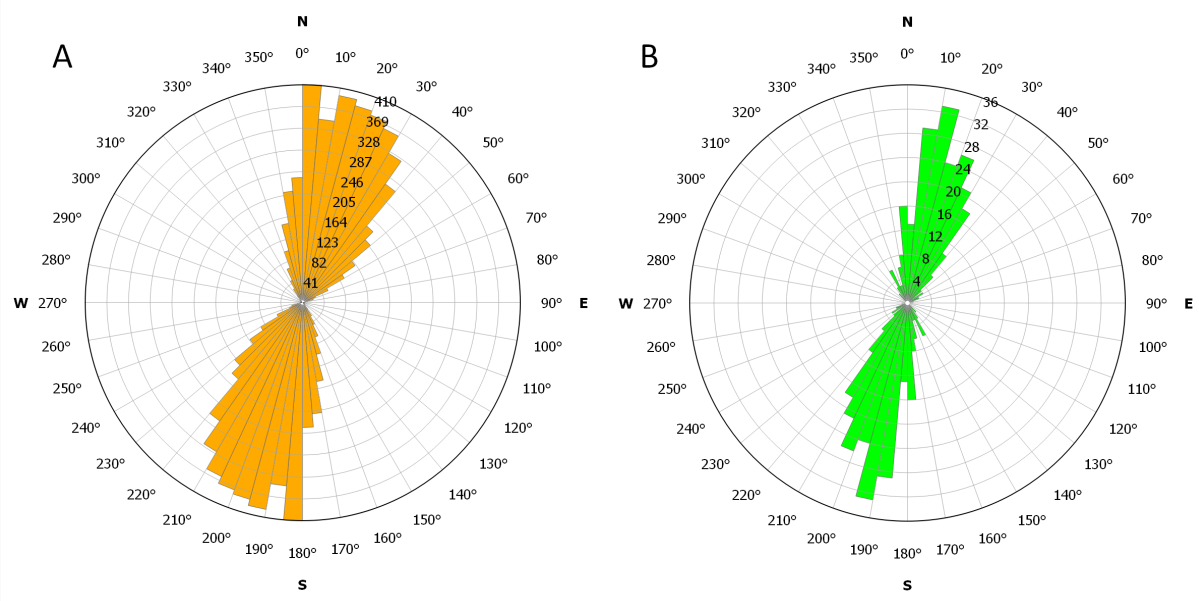
A
N
0°
10°
20°
30°
40°
50°
60°
70°
80°
90°
E
100°
110°
120°
130°
140°
150°
160°
170°
180°
S
190°
200°
210°
220°
230°
240°
250°
260°
W
270°
280°
290°
300°
310°
320°
330°
340°
350°
410
369
328
287
246
205
164
123
82
41
B
N
0°
10°
20°
30°
40°
50°
60°
70°
80°
90°
E
100°
110°
120°
130°
140°
150°
160°
170°
180°
S
190°
200°
210°
220°
230°
240°
250°
260°
W
270°
280°
290°
300°
310°
320°
330°
340°
350°
36
32
28
24
20
16
12
8
4

Fig. S2